

## 1 **Structure-based modeling of SARS-CoV-2 peptide/HLA-A02 antigens**

2

3 Santrupti Nerli<sup>1</sup> and Nikolaos G. Sgourakis<sup>2</sup>

4 Email: [nsgourak@ucsc.edu](mailto:nsgourak@ucsc.edu)

5

6 <sup>1</sup>Department of Biomolecular Engineering, University of California Santa Cruz, Santa Cruz, CA  
7 95064, USA.

8 <sup>2</sup>Department of Chemistry and Biochemistry, University of California Santa Cruz, Santa Cruz, CA  
9 95064, USA.

10

### 11 **ABSTRACT**

12 As a first step toward the development of diagnostic and therapeutic tools to fight the Coronavirus  
13 disease (COVID-19), it is important to characterize CD8<sup>+</sup> T cell epitopes in the SARS-CoV-2  
14 peptidome that can trigger adaptive immune responses. Here, we use RosettaMHC, a comparative  
15 modeling approach which leverages existing high-resolution X-ray structures from peptide/MHC  
16 complexes available in the Protein Data Bank, to derive physically realistic 3D models for high-  
17 affinity SARS-CoV-2 epitopes. We outline an application of our method to model 439 9mer and  
18 279 10mer predicted epitopes displayed by the common allele HLA-A\*02:01, and we make our  
19 models publicly available through an online database (<https://rosettamhc.chemistry.ucsc.edu>). As  
20 more detailed studies on antigen-specific T cell recognition become available, RosettaMHC  
21 models of antigens from different strains and HLA alleles can be used as a basis to understand the  
22 link between peptide/HLA complex structure and surface chemistry with immunogenicity, in the  
23 context of SARS-CoV-2 infection.

24

25 An ongoing pandemic caused by the novel SARS coronavirus (SARS-CoV-2) has become the  
26 focus of extensive efforts to develop vaccines and antiviral therapies (1). Immune modulatory  
27 interferons, which promote a widespread antiviral reaction in infected cells, and inhibition of pro-  
28 inflammatory cytokine function through anti-IL-6/IL-6R antibodies, have been proposed as  
29 possible COVID-19 therapies (2, 3). However, stimulating a targeted T cell response against  
30 specific viral antigens is hampered by a lack of detailed knowledge of the immunodominant  
31 epitopes displayed by common Human Leukocyte Antigen (HLA) alleles across individuals  
32 (public epitopes). The molecules of the class I major histocompatibility complex (MHC-I, or HLA  
33 in humans) display on the cell surface a diverse pool of 8 to 15 amino acid peptides derived from  
34 the endogenous processing of proteins expressed inside the cell (4). This MHC-I restriction of  
35 peptide antigens provides jawed vertebrates with an essential mechanism for adaptive immunity:  
36 surveillance of the displayed peptide/MHC-I (pMHC-I) molecules by CD8<sup>+</sup> cytotoxic T-  
37 lymphocytes allows detection of aberrant protein expression patterns, which signify viral infection  
38 and can trigger an adaptive immune response (5). A recent study has shown important changes in  
39 T cell compartments during the acute phase of SARS-CoV-2 infection (6), suggesting that the  
40 ability to quantify antigen-specific T cells would provide new avenues for understanding the

41 expansion and contraction of the TCR repertoire in different disease cohorts and clinical settings.  
42 Given the reduction in breadth and functionality of the naïve T cell repertoire during aging (7),  
43 identifying a minimal set of viral antigens that can elicit a protective response will enable the  
44 design of diagnostic tools to monitor critical gaps in the T cell repertoire of high-risk cohorts,  
45 which can be addressed using peptide or epitope string DNA vaccines (8).  
46 Human MHC-I molecules are extremely polymorphic, with thousands of known alleles in the  
47 classical HLA-A, -B and -C loci. Specific amino acid polymorphisms along the peptide-binding  
48 groove (termed A-F pockets) define a repertoire of  $10^4$ - $10^6$  peptide antigens that can be recognized  
49 by each HLA allotype (9, 10). Several machine-learning methods have been developed to predict  
50 the likelihood that a target peptide will bind to a given allele (reviewed in (11)). Generally these  
51 methods make use of available data sets in the Immune Epitope Database (12) to train artificial  
52 neural networks that predict peptide processing, binding and display, and their performance varies  
53 depending on peptide length and HLA allele representation in the database. Structure-based  
54 approaches have also been proposed to model the bound peptide conformation *de novo* (reviewed  
55 in (13)). These approaches utilize various algorithms to optimize the backbone and side chain  
56 degrees of freedom of the peptide/MHC structure according to an all-atom scoring function,  
57 derived from physical principles (14–16), that can be further enhanced using modified scoring  
58 terms (17) or mean field theory (18). While these methods do not rely on large training data sets,  
59 their performance is affected by bottlenecks in sampling of different backbone conformations, and  
60 any possible structural adaptations of the HLA peptide-binding groove.  
61 Predicting the bound peptide conformation whose N- and C- termini are anchored within a fixed-  
62 length groove is a tractable modeling problem that can be addressed using standard comparative  
63 modeling approaches (19). In previous work focusing on the HLA-B\*15:01 and HLA-A\*01:01  
64 alleles in the context of neuroblastoma neoantigens, we have found that a combined backbone and  
65 side chain optimization approach can yield accurate pMHC-I models for a pool of target peptides,  
66 provided that a reliable template of the same allele and peptide length can be identified in the  
67 database (20). In this approach (RosettaMHC), a local optimization of the backbone degrees of  
68 freedom is sufficient to capture minor (within 0.5 Å heavy atom RMSD) changes of the target  
69 peptide backbone relative to the conformation of the peptide in the template, used as a starting  
70 point. For HLA-A\*02:01, the most common HLA allele among disease-relevant population  
71 cohorts (21), there is a large number of high-resolution X-ray structures available in the PDB (22),  
72 suggesting that a similar principle can be applied to produce models of candidate epitopes directly  
73 from the proteome of a pathogen of interest. Here, we apply RosettaMHC to all HLA-A\*02:01  
74 epitopes predicted directly from the ~30 kbp SARS-CoV-2 genome, and make our models publicly  
75 available through an online database. The computed binding energies of our models can be used  
76 as an additional validation layer to select high-affinity epitopes from large peptide sets. As detailed  
77 epitope mapping data from high-throughput tetramer staining (23–25) and T cell functional  
78 screens (26) become available, the models presented here can provide a toehold for understanding  
79 links between pMHC-I antigen structure and immunogenicity, with actionable value for the  
80 development of peptide vaccines to combat the disease.

## 81 **Materials and Methods**

### 82 *Identification of SARS-CoV-2 peptide epitopes*

83 The SARS-CoV-2 protein sequences ([https://www.ncbi.nlm.nih.gov/nucore/NC\\_045512.2](https://www.ncbi.nlm.nih.gov/nucore/NC_045512.2)) were  
84 obtained from NCBI and used to generate all possible peptides of lengths 9 and 10 (9,621 9mer  
85 and 9,611 10mer peptides). We used NetMHCpan-4.0 (27) to derive binding scores to HLA-  
86 A\*02:01, and retained only peptides classified as strong or weak binders (selected using the default  
87 percentile rank cut-off values). The binding classification was performed using eluted ligand  
88 likelihood predictions. While in this study we use NetMHCpan-4.0 predictions as inputs to select  
89 candidate epitopes for structure modeling, our workflow is fully compatible with any alternative  
90 epitope prediction method.

91

### 92 *Selection of PDB templates*

93 To model SARS-CoV-2 / HLA-A\*02:01 antigens, we identified 3D structures from the PDB that  
94 can be used as templates for comparative modeling. First, we selected all HLA-A02 X-ray  
95 structures that are below 3.5 Å resolution and retained only those that have 100% identity to the  
96 HLA-A\*02:01 heavy chain sequence (residues 1-180). We found 241 template structures bound  
97 to epitopes of lengths from 8 to 15 residues (of which 170 are 9mers and 61 are 10mers). For each  
98 SARS-CoV-2 target peptide, we selected a set of candidate templates of the same length by  
99 matching the target peptide anchor positions (P2 and P9/P10) to each peptide in the template  
100 structures. Then, we used the BLOSUM62 (28) substitution matrix to score all remaining positions  
101 in the pairwise alignment of the target/template sequences, and the PDB template with the top  
102 alignment score was selected for modeling. For target peptides where we found no templates which  
103 match both peptide anchors, we scored all positions in the pairwise alignment and selected the top  
104 scoring template for modeling.

105

### 106 *RosettaMHC modeling framework and database*

107 RosettaMHC (manuscript in preparation) is a comparative modeling protocol developed using  
108 PyRosetta (29) to model pMHC-I complexes. The program accepts as input a list of peptide  
109 sequences, an HLA allele definition and a template PDB file (selected as described in the previous  
110 step). To minimize "noise" in the simulation from parts of the MHC-I fold that do not contribute  
111 to peptide binding, only the  $\alpha_1$  and  $\alpha_2$  domains are considered in all steps. For each peptide, a full  
112 alignment between the target and template peptide/MHC sequences is performed using clustal  
113 omega (30). The alignment is used as input to Rosetta's threading protocol (*partial\_thread.<ext>*).  
114 From the threaded model, all residues in the MHC-I groove that are within a heavy-atom distance  
115 of 3.5 Å from the peptide are subjected to 10 independent all-atom refinement simulations using  
116 the FastRelax method (31) and a custom movemap file. Binding energies are extracted from the  
117 refined structures using interface analyzer protocol (*InterfaceAnalyzer.<ext>*). The top three  
118 models are selected based on the binding energies, and used to compute an average energy for  
119 each peptide in the input list. RosettaMHC models of SARS-CoV-2/HLA-A\*02:01 epitopes are

120 made available through an online database (see data availability). The website that hosts our  
121 database was constructed using the Django web framework.

122

123

## 124 **Results and Discussion**

125

### 126 *Template identification for structure modeling using RosettaMHC*

127 Our full workflow for template identification and structure modeling is outlined in Figure 1a, with  
128 a flowchart shown in Figure 1b. To identify all possible regular peptide binders to HLA-A\*02:01  
129 that are expressed by SARS-CoV-2, we used a recently annotated version of all open reading  
130 frames (ORFs) in the viral genome from NCBI (32), made available through the UCSC genome  
131 browser (33). We used 9- and 10- residue sliding windows to scan all protein sequences, since  
132 these are the optimum peptide lengths for binding to the HLA-A\*02:01 groove (34). While spliced  
133 peptide epitopes (35) are not considered in the current study, this functionality can be added to our  
134 method at a later stage. Using NetMHCpan-4.0 (27), we identified all 439 9mer and 279 10mer  
135 epitopes that are predicted to yield positive (classified as both weak and strong) binders. To further  
136 validate this set and derive plausible 3D models of the peptide/HLA-A\*02:01 complexes, we used  
137 a structure-guided approach, RosettaMHC, which aims to derive a physically realistic fitness score  
138 for each peptide in the HLA-A\*02:01 binding groove using an annotated database of high-  
139 resolution structures and Rosetta's all-atom energy function (36). RosettaMHC leverages a  
140 database of 241 HLA-A\*02:01 X-ray structures encompassing a range of bound peptides, to find  
141 the closest match to each target epitope predicted from the SARS-CoV-2 proteome. To identify  
142 the best template for structure modeling, we use sequence matching criteria which first consider  
143 the peptide anchors (positions P2 and P9/P10 for 9mer/10mer epitopes), followed by a sequence  
144 similarity metric calculated from the full alignment between the template and target peptide  
145 sequences. The template assignment statistics for the four different classes of SARS-CoV-2  
146 epitopes in our set are shown in Figure 2a. We find that we can cover the entire set of 718 predicted  
147 binders using a subset of 114 HLA-A\*02:01 templates in our annotated database of PDB-derived  
148 structures (Figure 2b). Each target peptide sequence is then threaded onto the backbone of its best  
149 identified template, followed by all-atom refinement of the side chain and backbone degrees of  
150 freedom using Rosetta's Ref2015 energy function (36), and binding energy calculation.

151

### 152 *RosettaMHC models recapitulate features of high-resolution X-ray structures*

153 The sequence logos derived from 9mer and 10mer peptides with good structural complementarity  
154 to the HLA-A\*02:01 groove according to Rosetta's binding energy (see below) adhere to the  
155 canonical motif, with a preference for hydrophobic, methyl-bearing side chains at the peptide  
156 anchor residues P2 and P9 (Figure 3a). The anchor residue preferences are recapitulated in  
157 representative 9mer and 10mer models of the two top binders in our set as ranked by Rosetta's  
158 energy (Figure 3c and 3d), corresponding to epitopes TMADLVYAL and FLFVAAIFYL derived  
159 from the RNA polymerase and nsp3 proteins, respectively, which are both encoded by *orf1ab* in

160 the viral genome (NCBI Reference YP\_009724389.1). In accordance with features seen in high-  
161 resolution structures of HLA-A\*02:01-restricted epitopes, the peptides adopt an extended, bulged  
162 backbone conformation. The free N-terminus of both peptides is stabilized by a network of polar  
163 contacts with Tyr 7, Tyr 159, Tyr 171 and Glu 63 in the A- and B- pockets of the HLA-A\*02:01  
164 groove. The Met (9mer) or Leu (10mer) side chain of P2 is buried in a B-pocket hydrophobic cleft  
165 formed by Met 45 and Val 67. Equivalently, the C-terminus is coordinated through polar contacts  
166 with Asp 77 and Lys 145 from opposite sides of the groove, with the Leu P9/P10 anchor nestled  
167 in the F-pocket defined by the side chains of Leu 81, Tyr 116, Tyr 123 and Trp 147. Residues P3-  
168 P8 form a series of backbone and side chain contacts with pockets C, D and E, while most  
169 backbone amide and carbonyl groups form hydrogen bonds with the side chains of residues lining  
170 the MHC-I groove. These high-resolution structural features are consistent across low-energy  
171 models of unrelated target peptides in our input set, suggesting that, when provided with a large  
172 set of input templates, a combined threading and side chain optimization protocol can derive  
173 physically realistic models.

174

#### 175 *Selection of high-affinity peptide epitopes using a structure-based score*

176 To evaluate the accuracy of our models and fitness of each peptide within the HLA-A\*02:01  
177 binding groove, we computed Rosetta all-atom binding energies across all complexes modeled for  
178 different peptide sets. High binding energies can be used as an additional metric to filter low-  
179 affinity peptides in the NetMHCpan-4.0 predictions, with the caveat that high energies can be also  
180 due to incomplete optimization of the Rosetta energy function as a result of significant deviations  
181 between the target and template backbone conformations, not captured by our protocol. We  
182 performed 10 independent calculations for each peptide, and the 3 lower-energy models were  
183 selected as the final ensemble and used to compute an average binding energy. The results for all  
184 9mer peptides are summarized in Figures 3e, f, while additional results for 10mers are provided  
185 through our web-interface and outlined in Supplemental Table 1. As a positive reference, we used  
186 the binding energies of the idealized and relaxed PDB templates, which are at a local minimum of  
187 the Rosetta scoring function. As a reference set for sub-optimal binders, we modeled decoy  
188 structures of poly alanine (polyA) peptide sequences (predicted by NetMHCpan-4.0 to be a top  
189 9th percentile binder for HLA-A\*02:01), threaded onto the same PDB templates.

190

191 We observe a significant, negative (-26 kcal/mol) energy gap between the average binding energies  
192 for PDB templates and poly alanine models. The binding energies for all modeled 9mers from the  
193 SARS-CoV-2 genome fall between the average energies of the optimal PDB templates and sub-  
194 optimal polyA binders, and show a bimodal distribution with significant overlap with the refined  
195 PDB template energies (Figure 1e). Comparison of the distributions between epitopes that are  
196 classified as strong versus weak binders by NetMHCpan-4.0 shows a moderate bias towards lower  
197 binding energies for the strong binders and a larger spread in energies for weak binders, likely due  
198 to suboptimal residues at the P2 and P9 anchor positions (Figure 3f). As an intended positive set,  
199 we also modeled 28 9mer peptides that are homologous to peptides in the SARS viral genome and

200 have been previously reported to bind HLA-A\*02:01 in the IEDB and ViPR (12, 37, 38) databases  
201 (Supplemental Table 2). Inspection of Rosetta binding energies derived from models in this set  
202 shows a similar distribution to the epitopes classified by NetMHCpan-4.0 as strong binders, with  
203 the energies of 19/28 peptides falling well within the distribution of the refined PDB templates  
204 (red dots in Figure 3e).

205  
206 Based on these observations, we further classified all epitopes in the original set provided by  
207 NetMHCpan-4.0 as strong or weak binders according to the Rosetta binding energy. Peptides with  
208 binding energies that fall well within the PDB template distribution (green curve and red dots in  
209 Figure 3e) are classified as strong binders. We obtained 154 9mer and 72 10mer strong binders  
210 which show optimal complementarity within the HLA-A\*02:01 peptide-binding groove according  
211 to our modeling simulations. These results suggest that the high-resolution features seen in our  
212 models (Figure 3c, d) yield optimal binding energies for a significant fraction of the epitopes  
213 predicted by NetMHCpan-4.0 (45/33% of strong binders and 30/25% of weak binders for  
214 9mers/10mers, respectively), which are comparable to locally refined PDB structures. The average  
215 binding energies for all peptides are provided in our web-interface and in Supplemental Table 1.

216

#### 217 *Surface features of peptide/HLA-A\*02:01 models for T cell recognition*

218 Visualization of our models through an interactive online interface provides direct information on  
219 SARS-CoV-2 peptide residues that are bulging out of the MHC-I groove, and are therefore  
220 accessible to interactions with complementarity-determining regions (CDRs) of T cell receptors  
221 (TCRs). Given that  $\alpha\beta$  TCRs generally employ a diagonal binding mode to engage pMHC-I  
222 antigens where the CDR3 $\alpha$  and CDR3 $\beta$  TCR loops form direct contacts with key peptide residues  
223 (39, 40), knowledge of the surface features for different epitopes adds an extra layer of information  
224 to interpret sequence variability between different viral strains. For other important antigens with  
225 known structures in the PDB, such features can be derived from an annotated database connecting  
226 pMHC-I/TCR co-crystal structures with biophysical binding data (41), and were recently  
227 employed in an artificial neural network approach to predict the immunogenicity of different HLA-  
228 A\*02:01 bound peptides in the context of tumor neoantigen display (42). A separate study has  
229 shown that the electrostatic compatibility between self vs foreign HLA surfaces can be used to  
230 determine antibody alloimmune responses (43). Given that antibodies and TCRs use a common  
231 fold and similar principles to engage pMHC-I molecules (40), it is likely that surface electrostatic  
232 features play an important role in recognition of peptide/HLA surfaces by their cognate TCRs in  
233 the context of SARS-CoV-2 infection.

234 Electrostatic surface potentials calculated using a numerical solution to the Poisson-Boltzmann  
235 Equation (44) for our modeled peptide/HLA-A\*02:01 complexes allow us to compare important  
236 features for TCR recognition between different high-affinity epitopes (Figure 4). We observe a  
237 moderate electropositive character of the HLA-A\*02:01  $\alpha_1$  helix, and a moderate negative  
238 potential on the  $\alpha_2$  helix, which is consistent between complexes with different bound peptides.  
239 However, due to substantial sequence variability in surface-exposed residues at the P2-P8

240 positions, we observe a range of electrostatic features ranging from negative (epitope  
241 TMADLVYAL), to neutral (NLIDSYFVV) or positively charged (KLWAQCVQL). Further  
242 classification and ranking of the top binders in our set on the basis of their molecular surface  
243 features would enable the selection of the most diverse panel of peptides for high-throughput  
244 pMHC tetramer library generation (23-25). Tetramer screening of T cells from COVID-19  
245 patients, recovered individuals and healthy donors can be used to identify critical gaps in the T cell  
246 repertoire of high-risk groups, and to design epitope DNA strings for vaccine development.

247

### 248 **Acknowledgements**

249 The authors are grateful to Alison Lindberg and ITS/ADC staff at UCSC for assistance in setting  
250 up the web server for the database, and Hiram Clawson (UCSC Genome Browser) for providing  
251 the SARS-CoV-2 protein sequence data. We thank Andrew McShan, Hailey Wallace (UCSC) for  
252 assistance in the development of the RosettaMHC protocol, and David Haussler (UCSC), Michael  
253 Betts (University of Pennsylvania) and David Margulies (NIH) for helpful discussions. This work  
254 was supported through Grants from NIAID (5R01AI143997) and NIGMS (5R35GM125034).

255

### 256 **Code and Data availability**

257 An online web-interface for visualization and download of all models is available at:  
258 <https://rosettamhc.chemistry.ucsc.edu>. The RosettaMHC source code is available at  
259 <https://github.com/snerligit/mhc-pep-threader>. Rosetta binding energies for all 718 HLA-  
260 A\*02:01-restricted peptides in our set are provided in Supplemental Table 1.

261

### 262 **Disclosures**

263 The authors have no financial conflicts of interest.

264

### 265 **References**

- 266 1. Liu, C., Q. Zhou, Y. Li, L. V. Garner, S. P. Watkins, L. J. Carter, J. Smoot, A. C. Gregg, A. D.  
267 Daniels, S. Jervy, and D. Albaiu. 2020. Research and Development on Therapeutic Agents and  
268 Vaccines for COVID-19 and Related Human Coronavirus Diseases. *ACS Cent. Sci.* .
- 269 2. Kumaki, Y., J. Ennis, R. Rahbar, J. D. Turner, M. K. Wandersee, A. J. Smith, K. W. Bailey, Z.  
270 G. Vest, J. R. Madsen, J. K.-K. Li, and D. L. Barnard. 2011. Single-dose intranasal  
271 administration with mDEF201 (adenovirus vectored mouse interferon-alpha) confers protection  
272 from mortality in a lethal SARS-CoV BALB/c mouse model. *Antiviral Res.* 89: 75–82.
- 273 3. Kishimoto, T. 2006. Interleukin-6: discovery of a pleiotropic cytokine. *Arthritis Res. Ther.* 8:  
274 S2.
- 275 4. Rock, K. L., E. Reits, and J. Neefjes. 2016. Present Yourself! By MHC Class I and MHC  
276 Class II Molecules. *Trends Immunol.* 37: 724–737.
- 277 5. Kaufman, J. 2018. Unfinished Business: Evolution of the MHC and the Adaptive Immune  
278 System of Jawed Vertebrates. *Annu. Rev. Immunol.* 36: 383–409.
- 279 6. Thevarajan, I., T. H. O. Nguyen, M. Koutsakos, J. Druce, L. Caly, C. E. van de Sandt, X. Jia,  
280 S. Nicholson, M. Catton, B. Cowie, S. Y. C. Tong, S. R. Lewin, and K. Kedzierska. 2020.

- 281 Breadth of concomitant immune responses prior to patient recovery: a case report of non-severe  
282 COVID-19. *Nat. Med.* 1–3.
- 283 7. Goronzy, J. J., F. Fang, M. M. Cavanagh, Q. Qi, and C. M. Weyand. 2015. Naïve T cell  
284 maintenance and function in human aging. *J. Immunol. Baltim. Md 1950* 194: 4073–4080.
- 285 8. Oyarzun, P., and B. Kobe. 2015. Computer-aided design of T-cell epitope-based vaccines:  
286 addressing population coverage. *Int. J. Immunogenet.* 42: 313–321.
- 287 9. Birnbaum, M. E., J. L. Mendoza, D. K. Sethi, S. Dong, J. Glanville, J. Dobbins, E. Ozkan, M.  
288 M. Davis, K. W. Wucherpfennig, and K. C. Garcia. 2014. Deconstructing the peptide-MHC  
289 specificity of T cell recognition. *Cell* 157: 1073–1087.
- 290 10. Wooldridge, L., J. Ekeruche-Makinde, H. A. van den Berg, A. Skowera, J. J. Miles, M. P.  
291 Tan, G. Dolton, M. Clement, S. Llewellyn-Lacey, D. A. Price, M. Peakman, and A. K. Sewell.  
292 2012. A single autoimmune T cell receptor recognizes more than a million different peptides. *J.*  
293 *Biol. Chem.* 287: 1168–1177.
- 294 11. Peters, B., M. Nielsen, and A. Sette. 2020. T Cell Epitope Predictions. *Annu. Rev. Immunol.* .
- 295 12. Vita, R., S. Mahajan, J. A. Overton, S. K. Dhanda, S. Martini, J. R. Cantrell, D. K. Wheeler,  
296 A. Sette, and B. Peters. 2019. The Immune Epitope Database (IEDB): 2018 update. *Nucleic*  
297 *Acids Res.* 47: D339–D343.
- 298 13. Antunes, D. A., J. R. Abella, D. Devaurs, M. M. Rigo, and L. E. Kavraki. 2018. Structure-  
299 based Methods for Binding Mode and Binding Affinity Prediction for Peptide-MHC Complexes.  
300 *Curr. Top. Med. Chem.* 18: 2239–2255.
- 301 14. Yanover, C., and P. Bradley. 2011. Large-scale characterization of peptide-MHC binding  
302 landscapes with structural simulations. *Proc. Natl. Acad. Sci.* 108: 6981–6986.
- 303 15. King, C., E. N. Garza, R. Mazor, J. L. Linehan, I. Pastan, M. Pepper, and D. Baker. 2014.  
304 Removing T-cell epitopes with computational protein design. *Proc. Natl. Acad. Sci. U. S. A.* 111:  
305 8577–8582.
- 306 16. Liu, T., X. Pan, L. Chao, W. Tan, S. Qu, L. Yang, B. Wang, and H. Mei. 2014. Subangstrom  
307 accuracy in pHLA-I modeling by Rosetta FlexPepDock refinement protocol. *J. Chem. Inf.*  
308 *Model.* 54: 2233–2242.
- 309 17. Kyeong, H.-H., Y. Choi, and H.-S. Kim. 2018. GradDock: rapid simulation and tailored  
310 ranking functions for peptide-MHC Class I docking. *Bioinformatics* 34: 469–476.
- 311 18. Rubenstein, A. B., M. A. Pethe, and S. D. Khare. 2017. MFPred: Rapid and accurate  
312 prediction of protein-peptide recognition multispecificity using self-consistent mean field theory.  
313 *PLoS Comput. Biol.* 13: e1005614.
- 314 19. Song, Y., F. DiMaio, R. Y.-R. Wang, D. Kim, C. Miles, T. Brunette, J. Thompson, and D.  
315 Baker. 2013. High-Resolution Comparative Modeling with RosettaCM. *Structure* 21: 1735–  
316 1742.
- 317 20. Frontiers | A Recurrent Mutation in Anaplastic Lymphoma Kinase with Distinct Neoepitope  
318 Conformations | Immunology. .
- 319 21. Robinson, J., L. A. Guethlein, N. Cereb, S. Y. Yang, P. J. Norman, S. G. E. Marsh, and P.  
320 Parham. 2017. Distinguishing functional polymorphism from random variation in the sequences  
321 of >10,000 HLA-A, -B and -C alleles. *PLoS Genet.* 13.
- 322 22. Berman, H. M., J. Westbrook, Z. Feng, G. Gilliland, T. N. Bhat, H. Weissig, I. N.  
323 Shindyalov, and P. E. Bourne. 2000. The Protein Data Bank. *Nucleic Acids Res.* 28: 235–242.
- 324 23. Bentzen, A. K., A. M. Marquard, R. Lyngaa, S. K. Saini, S. Ramskov, M. Donia, L. Such, A.  
325 J. S. Furness, N. McGranahan, R. Rosenthal, P. T. Straten, Z. Szallasi, I. M. Svane, C. Swanton,  
326 S. A. Quezada, S. N. Jakobsen, A. C. Eklund, and S. R. Hadrup. 2016. Large-scale detection of

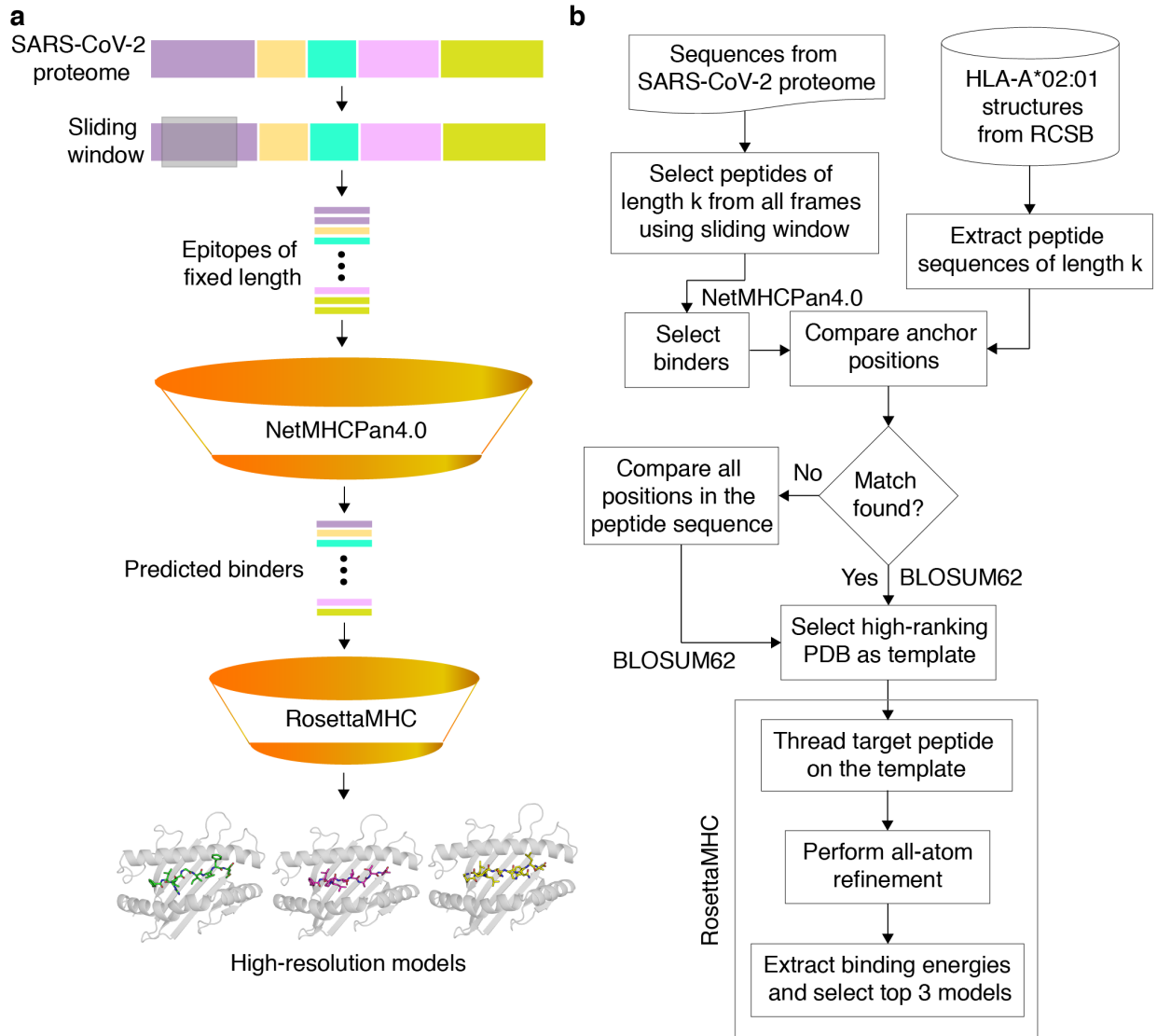


- 327 antigen-specific T cells using peptide-MHC-I multimers labeled with DNA barcodes. *Nat.*  
328 *Biotechnol.* 34: 1037–1045.
- 329 24. Saini, S. K., T. Tamhane, R. Anjanappa, A. Saikia, S. Ramskov, M. Donia, I. M. Svane, S. N.  
330 Jakobsen, M. Garcia-Alai, M. Zacharias, R. Meijers, S. Springer, and S. R. Hadrup. 2019. Empty  
331 peptide-receptive MHC class I molecules for efficient detection of antigen-specific T cells. *Sci.*  
332 *Immunol.* 4.
- 333 25. Overall, S. A., J. S. Toor, S. Hao, M. Yarmarkovich, S. M. O'Rourke, G. I. Morozov, S.  
334 Nguyen, A. S. Japp, N. Gonzalez, D. Moschidi, M. R. Betts, J. M. Maris, P. Smibert, and N. G.  
335 Sgourakis. High Throughput pMHC-I Tetramer Library Production Using Chaperone-Mediated  
336 Peptide Exchange. *Nat. Commun. Press* .
- 337 26. Ishizuka, J., K. Grebe, E. Shenderov, B. Peters, Q. Chen, Y. Peng, L. Wang, T. Dong, V.  
338 Pasquetto, C. Oseroff, J. Sidney, H. Hickman, V. Cerundolo, A. Sette, J. R. Bennink, A.  
339 McMichael, and J. W. Yewdell. 2009. Quantitating T Cell Cross-Reactivity for Unrelated  
340 Peptide Antigens. *J. Immunol.* 183: 4337–4345.
- 341 27. Jurtz, V., S. Paul, M. Andreatta, P. Marcatili, B. Peters, and M. Nielsen. 2017. NetMHCpan-  
342 4.0: Improved Peptide-MHC Class I Interaction Predictions Integrating Eluted Ligand and  
343 Peptide Binding Affinity Data. *J. Immunol. Baltim. Md 1950* 199: 3360–3368.
- 344 28. Henikoff, S., and J. G. Henikoff. 1992. Amino acid substitution matrices from protein blocks.  
345 *Proc. Natl. Acad. Sci. U. S. A.* 89: 10915–10919.
- 346 29. Chaudhury, S., S. Lyskov, and J. J. Gray. 2010. PyRosetta: a script-based interface for  
347 implementing molecular modeling algorithms using Rosetta. *Bioinformatics* 26: 689–691.
- 348 30. Sievers, F., A. Wilm, D. Dineen, T. J. Gibson, K. Karplus, W. Li, R. Lopez, H. McWilliam,  
349 M. Remmert, J. Söding, J. D. Thompson, and D. G. Higgins. 2011. Fast, scalable generation of  
350 high-quality protein multiple sequence alignments using Clustal Omega. *Mol. Syst. Biol.* 7: 539.
- 351 31. Tyka, M. D., D. A. Keedy, I. André, F. Dimaio, Y. Song, D. C. Richardson, J. S. Richardson,  
352 and D. Baker. 2011. Alternate states of proteins revealed by detailed energy landscape mapping.  
353 *J. Mol. Biol.* 405: 607–618.
- 354 32. Wu, F., S. Zhao, B. Yu, Y.-M. Chen, W. Wang, Z.-G. Song, Y. Hu, Z.-W. Tao, J.-H. Tian,  
355 Y.-Y. Pei, M.-L. Yuan, Y.-L. Zhang, F.-H. Dai, Y. Liu, Q.-M. Wang, J.-J. Zheng, L. Xu, E. C.  
356 Holmes, and Y.-Z. Zhang. 2020. A new coronavirus associated with human respiratory disease in  
357 China. *Nature* 579: 265–269.
- 358 33. Kent, W. J., C. W. Sugnet, T. S. Furey, K. M. Roskin, T. H. Pringle, A. M. Zahler, and  
359 D. Haussler. 2002. The Human Genome Browser at UCSC. *Genome Res.* 12: 996–1006.
- 360 34. Trolle, T., C. P. McMurtrey, J. Sidney, W. Bardet, S. C. Osborn, T. Kaever, A. Sette, W. H.  
361 Hildebrand, M. Nielsen, and B. Peters. 2016. The length distribution of class I restricted T cell  
362 epitopes is determined by both peptide supply and MHC allele specific binding preference. *J.*  
363 *Immunol. Baltim. Md 1950* 196: 1480–1487.
- 364 35. Mishto, M., and J. Liepe. 2017. Post-Translational Peptide Splicing and T Cell Responses.  
365 *Trends Immunol.* 38: 904–915.
- 366 36. Alford, R. F., A. Leaver-Fay, J. R. Jeliazkov, M. O'Meara, F. P. DiMaio, H. Park, M. V.  
367 Shapovalov, P. D. Renfrew, V. K. Mulligan, K. Kappel, J. W. Labonte, M. S. Pacella, R.  
368 Bonneau, P. Bradley, R. L. Dunbrack Jr., R. Das, D. Baker, B. Kuhlman, T. Kortemme, and J. J.  
369 Gray. 2017. The Rosetta All-Atom Energy Function for Macromolecular Modeling and Design.  
370 *J. Chem. Theory Comput.* 13: 3031–3048.

- 371 37. Grifoni, A., J. Sidney, Y. Zhang, R. H. Scheuermann, B. Peters, and A. Sette. 2020. A  
372 Sequence Homology and Bioinformatic Approach Can Predict Candidate Targets for Immune  
373 Responses to SARS-CoV-2. *Cell Host Microbe* .
- 374 38. Pickett, B. E., E. L. Sadat, Y. Zhang, J. M. Noronha, R. B. Squires, V. Hunt, M. Liu, S.  
375 Kumar, S. Zaremba, Z. Gu, L. Zhou, C. N. Larson, J. Dietrich, E. B. Klem, and R. H.  
376 Scheuermann. 2012. ViPR: an open bioinformatics database and analysis resource for virology  
377 research. *Nucleic Acids Res.* 40: D593–D598.
- 378 39. Rossjohn, J., S. Gras, J. J. Miles, S. J. Turner, D. I. Godfrey, and J. McCluskey. 2015. T Cell  
379 Antigen Receptor Recognition of Antigen-Presenting Molecules. *Annu. Rev. Immunol.* 33: 169–  
380 200.
- 381 40. Rudolph, M. G., R. L. Stanfield, and I. A. Wilson. 2006. How TCRs bind MHCs, peptides,  
382 and coreceptors. *Annu. Rev. Immunol.* 24: 419–466.
- 383 41. Borrman, T., J. Cimons, M. Cosiano, M. Purcaro, B. G. Pierce, B. M. Baker, and Z. Weng.  
384 2017. ATLAS: A database linking binding affinities with structures for wild-type and mutant  
385 TCR-pMHC complexes. *Proteins Struct. Funct. Bioinforma.* 85: 908–916.
- 386 42. Riley, T. P., G. L. J. Keller, A. R. Smith, L. M. Davancaze, A. G. Arbuiso, J. R. Devlin, and  
387 B. M. Baker. 2019. Structure Based Prediction of Neoantigen Immunogenicity. *Front. Immunol.*  
388 10.
- 389 43. Mallon, D. H., C. Kling, M. Robb, E. Ellinghaus, J. A. Bradley, C. J. Taylor, D. Kabelitz,  
390 and V. Kosmoliaptsis. 2018. Predicting Humoral Alloimmunity from Differences in Donor and  
391 Recipient HLA Surface Electrostatic Potential. *J. Immunol.* 201: 3780–3792.
- 392 44. Baker, N. A., D. Sept, S. Joseph, M. J. Holst, and J. A. McCammon. 2001. Electrostatics of  
393 nanosystems: application to microtubules and the ribosome. *Proc. Natl. Acad. Sci. U. S. A.* 98:  
394 10037–10041.
- 395 45. Jurrus, E., D. Engel, K. Star, K. Monson, J. Brandi, L. E. Felberg, D. H. Brookes, L. Wilson,  
396 J. Chen, K. Liles, M. Chun, P. Li, D. W. Gohara, T. Dolinsky, R. Konecny, D. R. Koes, J. E.  
397 Nielsen, T. Head-Gordon, W. Geng, R. Krasny, G.-W. Wei, M. J. Holst, J. A. McCammon, and  
398 N. A. Baker. 2018. Improvements to the APBS biomolecular solvation software suite. *Protein*  
399 *Sci.* 27: 112–128.
- 400 46. *The PyMOL Molecular Graphics System*,. Schrödinger, LLC.
- 401
- 402

403 **FIGURES**

404

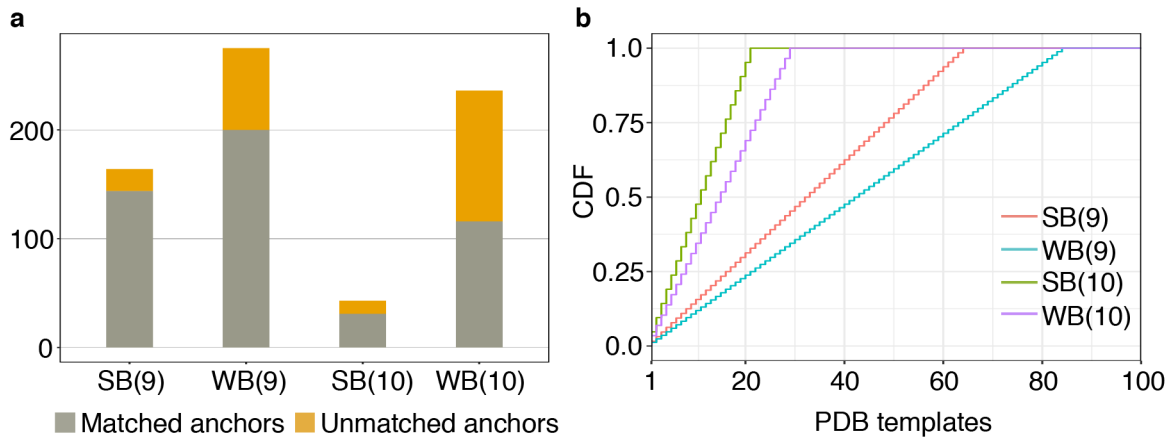


405

406 **FIGURE 1. Structure-guided modeling of T cell epitopes in the SARS-CoV-2 proteome**

407 **(a)** General workflow of our pipeline for structure-guided epitope ranking. **(b)** Protein sequences  
408 from the annotated SARS-CoV-2 proteome are used to generate peptide epitopes with a sliding  
409 window covering all frames of a fixed length (9,621 9mer and 9,611 10mer possible peptides).  
410 Candidate peptides are first filtered by NetMHCpan-4.0 (27) to identify all predicted strong and  
411 weak binders (439 9mer and 279 10mer epitopes). For rapid template matching and structure  
412 modeling, we use a local database of 241 HLA-A\*02:01 X-ray structures with resolution below  
413 3.5 Å from the Protein Data Bank (22). Each candidate peptide is scanned against all peptide  
414 sequences of the same length in the database, and the top-scoring template is used to guide the  
415 RosettaMHC comparative modeling protocol and to compute a binding energy.

416



417

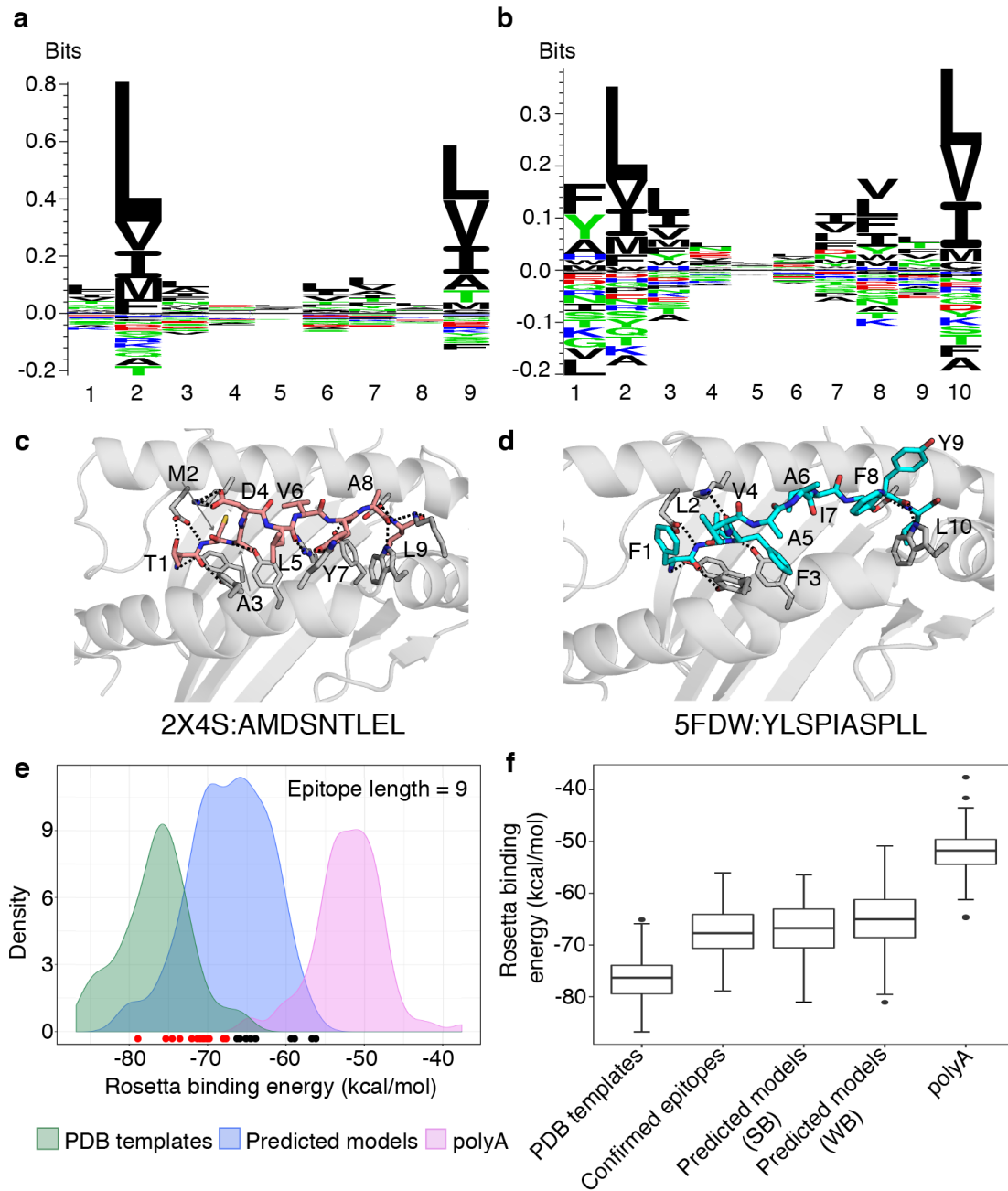
418 **FIGURE 2. Coverage of predicted HLA-A02 epitopes by structural templates in the PDB**

419 **(a)** Peptide anchor matching statistics of all predicted SARS-CoV-2 strong (SB) and weak binders

420 (WB) of lengths 9 and 10 to a database of 241 high-resolution HLA-A\*02:01 X-ray structures **(b)**

421 Plot showing cumulative distribution (CDF) of strong and weak binder peptides of lengths 9 and

422 10, as a function of the total number of matching templates from the Protein Data Bank (22).



423

424 **FIGURE 3. Summary of RosettaMHC modeling results for SARS-CoV-2 peptide epitopes**

425 Sequence logos from the  $n$  top ranking epitopes in the SARS-CoV-2 genome, predicted by

426 NetMHCpan-4.0 (27) and further refined using RosettaMHC binding simulations are shown for:

427 (a) 9mers ( $n=154$ ) and (b) 10mers ( $n=72$ ). The top 9mer and 10mer epitopes in our refined set are

428 shown: (c) TMADLVYAL, from RNA polymerase and (d) FLFVAAIFYL, from nsp3. Dotted

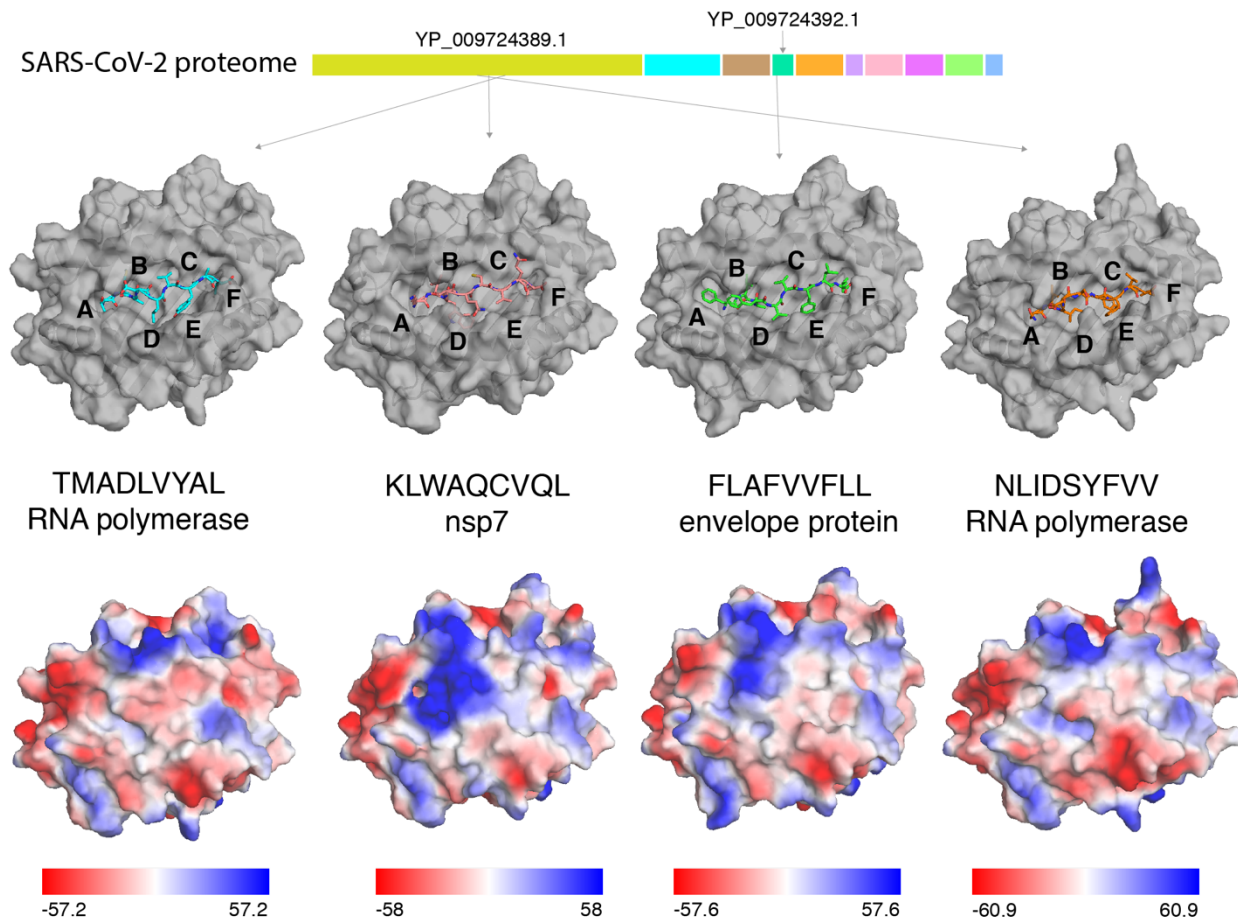
429 lines indicate polar contacts between peptide and heavy chain residues, with peptide residues

430 labelled. The template PDB IDs and original peptides used for modeling the target peptides are

431 indicated below each model. (e) Density plots showing distribution of average Rosetta binding

432 energies (kcal/mol) for all epitopes of length 9. Distributions reflect 93 PDB templates (green),

433 164 strong binder epitopes (according to NetMHCpan-4.0 (27)) (blue), and 93 poly alanine  
434 peptides modeled using the same PDB templates and used as a reference set for sub-optimal  
435 binders (polyA; pink). The binding energies of models generated for 28 confirmed SARS T cell  
436 epitopes from the IEDB and ViPR (37, 38) are indicated by circles at the bottom of the plot. Red  
437 circles (19/28) indicate epitopes that lie within the distribution of refined PDB templates and black  
438 circles (9/28) indicate epitopes that fall within the distribution of polyA (sub-optimal binders). **(f)**  
439 Box plots showing distribution of average binding energies for 93 PDB templates, 93 poly alanine  
440 peptides, 28 confirmed epitopes (37, 38) and RosettaMHC models for 164 strong (SB) and 275  
441 weak (WB) binder 9mer epitopes predicted from the SARS-CoV-2 proteome using NetMHCpan-  
442 4.0 (27).  
443



444  
445 **FIGURE 4. Variability in TCR recognition features of HLA-A02 with different high-affinity**  
446 **peptides.** Molecular surfaces of SARS-CoV-2/HLA-A\*02:01 RosettaMHC models are shown for  
447 four top-scoring epitopes (ranked by Rosetta binding energy from left to right) captured in the A,  
448 B, C, D, E and F pockets of the MHC-I groove (top panel). The origins of the peptide epitopes in  
449 the ~30 kbp SARS-CoV-2 genome are noted. Electrostatic surfaces computed for the same models  
450 are shown in the bottom panel. Solvent-accessible surface representation with electrostatic  
451 potential in the indicated ranges (down to  $-60$  kcal/(mol $\cdot e$ ) in red and up to  $+61$  kcal/(mol $\cdot e$ ) in  
452 blue) were calculated using the APBS solver (45) in Pymol (46). All calculations were performed  
453 at 150 mM ionic strength, 298.15 Kelvin, pH 7.2, protein dielectric 2.0, and solvent dielectric  
454 78.54. Electrostatic potentials are given in units of kT/e. A 1.4 Å solvent (probe) radius and 10.0  
455 points/Å<sup>2</sup> density was used to calculate molecular surfaces.  
456